

Article

Paramagnetic iron-doped hydroxyapatite nanoparticles with improved metal sorption properties. A Bio-organic substrates-mediated synthesis.

D. Fabio Mercado, Giuliana Magnacca, Mery Malandrino, Aldo A. Rubert, Enzo Montoneri, Luisella Celi, Alessandra Bianco Prevot, and Monica C. Gonzalez

ACS Appl. Mater. Interfaces, **Just Accepted Manuscript** • DOI: 10.1021/am405217j • Publication Date (Web): 21 Feb 2014

Downloaded from <http://pubs.acs.org> on February 21, 2014

Just Accepted

“Just Accepted” manuscripts have been peer-reviewed and accepted for publication. They are posted online prior to technical editing, formatting for publication and author proofing. The American Chemical Society provides “Just Accepted” as a free service to the research community to expedite the dissemination of scientific material as soon as possible after acceptance. “Just Accepted” manuscripts appear in full in PDF format accompanied by an HTML abstract. “Just Accepted” manuscripts have been fully peer reviewed, but should not be considered the official version of record. They are accessible to all readers and citable by the Digital Object Identifier (DOI®). “Just Accepted” is an optional service offered to authors. Therefore, the “Just Accepted” Web site may not include all articles that will be published in the journal. After a manuscript is technically edited and formatted, it will be removed from the “Just Accepted” Web site and published as an ASAP article. Note that technical editing may introduce minor changes to the manuscript text and/or graphics which could affect content, and all legal disclaimers and ethical guidelines that apply to the journal pertain. ACS cannot be held responsible for errors or consequences arising from the use of information contained in these “Just Accepted” manuscripts.



Paramagnetic Iron-Doped Hydroxyapatite Nanoparticles with Improved Metal Sorption Properties. A Bio-Organic Substrates-Mediated Synthesis.

D. Fabio Mercado,^a Giuliana Magnacca,^b Mery Malandrino,^b Aldo Rubert,^a Enzo Montoneri,^b Luisella Celi,^c Alessandra Bianco Prevot,^b and Mónica C. Gonzalez^{*a}

^a Instituto de Investigaciones Fisicoquímicas Teóricas y Aplicadas (INIFTA), CCT-La Plata-CONICET, Universidad Nacional de La Plata, La Plata, Argentina.

^b Dipartimento di Chimica, Università di Torino, Via Giuria 7, Torino, Italy.

^c Dipartimento di Scienze Agrarie, Forestali e Alimentari, Università di Torino, Via Leonardo Da Vinci, 44 – Grugliasco, Torino, Italy.

• Corresponding author E-mail: gonzalez@inifta.unlp.edu.ar

Abstract

This paper describes the synthesis of paramagnetic iron-containing hydroxyapatite nanoparticles and their increased Cu²⁺ sorbent capacity when using Ca²⁺ complexes of soluble bio-organic substrates from urban wastes as synthesis precursors. A thorough characterization of the particles by TEM, XRD, FTIR spectroscopy, specific surface area, TGA, XPS, and DLS, indicates that loss of crystallinity, a higher specific area, an increased surface oxygen content, and formation of surface iron phases strongly enhance Cu²⁺ adsorption capacity of hydroxyapatite-based materials. However, the major effect of the surface and morphological modifications is the size diminution of the aggregates formed in aqueous solutions leading to an increased effective surface available for Cu²⁺ adsorption. Maximum sorption values of 550 - 850 mg Cu²⁺ per gram of particles suspended in an aqueous solution at pH 7 were determined; almost 10 times the maximum values observed for hydroxyapatite nanoparticles suspensions under the same conditions.

Keywords: Magnetic Nanomaterials; Cu²⁺ Sorption; Effective surface; Bio-Organic Substrates; Surface chemistry.

Introduction

Hydroxyapatite (Ap), Ca₁₀(PO₄)₆(OH)₂, the main component of the bone tissue of vertebrates, is one of the most promising sorbent materials for removing actinides and heavy metals from wastewaters and soils. Apatites of the most different origins, such as cow bone charcoal,¹ nano-Ap (nAp),² waste oyster shells,³ and bacteria,⁴ were used for the removal of heavy metals. Ap is an ideal material for long-term sequestration in aqueous reservoirs because of its chemical stability across a wide range of geological conditions,⁵ high biocompatibility, strong ability to fix actinides and heavy metals,⁶ and maximum metal ion sorption capacity

1
2
3 at pH 6 – 7.²

4 Humates are also widely applied to clean up toxic waste sites. Formation of humates is based on the ability
5 of carboxyl and hydroxyl groups of humic and/or fulvic acids to bind metal cations. In particular, Ca²⁺ are
6 effective precipitators of humates and provide a route for the transfer of trace metals from the solution to the
7 solid phase.⁷ Moreover, formation of stable, water-soluble phosphate-Ca²⁺-humic complexes⁸ were reported.
8 Urban bio-wastes (UBW) have been reported to contain soluble humic-like substances known as bioorganic
9 substances (SBO) which show promise as chemical auxiliaries for a number of technological applications in
10 the chemical industry and in environmental remediation.⁹ UBW-SBO are mixtures of substances with
11 molecular weights in the range (1–3)×10⁵ Da, formed by long aliphatic C chains substituted by aromatic
12 rings and COOH, NCO, C=O, PhOH, O-alkyl, O-aryl, OCO, OMe, and alkyl amines functional groups.
13 Therefore, the use of UBW-SBO as templates in the synthesis of Ap materials may be expected to affect Ap
14 morphology and surface chemistry, as observed for organic matrix-mediated fabrication of nanostructured
15 hydroxyapatite biocomposites.¹⁰

16
17
18
19
20
21
22
23
24
25
26
27
28
29
30
31
32
33
34
35
36
37
38
39
40
41
42
43
44
45
46
47
48
49
50
51
52
53
54
55
56
57
58
59
60

Nanomaterials showing high specific surface area and tunable surface chemistry were suggested to offer
significant improvement as metal adsorbents.¹¹ In particular, magnetite-incorporated hydroxyapatite
composites attract much attention as a magnetic functional material for developing adsorbents and catalysts
since they could be easily removed by application of a magnetic field.¹² However, to date, the metal
adsorption capacity of these materials was not assessed.

In this context, in the present communication we describe the synthesis of Ap-based magnetic nanoparticles
and their increased metal sorption capacity when synthesized using Ca²⁺ complexes of UBW-SBO as
synthesis precursors.

Experimental

Reactants

Calcium chloride 95 wt%, phosphoric acid 85%, FeCl₂·4H₂O > 99 %wt, FeCl₃·6H₂O 97 wt%, were supplied
by Sigma Aldrich and used without further purification. Deionized water was Milli-Q purified (18.2 MΩcm
and 6 ppb TOC). When required, pH was stabilized to 7.0 with 4-(2-hydroxyethyl)piperazine-1-
ethanesulfonic acid, sodium salt (HEPES-Na) and nitric acid.

The biorganic substances herein used were available from a pilot plant from Studio Chiono&Associati in
Rivarolo Canavese, Italy. The fraction of soluble biorganic substances used, namely CVT230, was extracted
from home gardening and park trimming residues aerated for 230 days for aerobic microbiological treatment;
the resulting biomass was digested with an alkali solution at 65 °C for several hours and the remaining
supernatant filtered by an UF membrane operating with tangential flow to yield a retentate with 5-10 % dry
matter content. The concentrated retentate (CVT230) was finally dried at 60 °C. CVT230 was 72.1% solid
residue, and composed of 38.25 ± 0.09 % w/w C and 4.01 ± 0.03 % w/w N. Among the important mineral
residues are: 256 ppm Zn, 202 ppm Cu, 92 ppm Ni, 85 ppm Pb, 19 ppm Cr, and minor amounts of Si, Fe,
and Ca. CVT230 carbon fractions are: 37% alifatic, 20 % aromatic, 14% alkoxy, 12 % carboxylic, and 7%

1
2
3 are in an α position to amines.¹³ SBO were reported to be non-toxic to *Vibrio Fischeri*, activated sludge
4 bacteria, *Daphnia magna*, and *Pseudokirchneriella subcapitata*. Their reported biological to chemical
5 oxygen demand ratio, BOD:COD < 0.1, indicates an extremely low biodegradability.
6

7 Addition of excess Ca^{2+} to SBO aqueous solutions of pH 11 leads to the formation of insoluble SBO- Ca^{2+}
8 products which became solubilized on decreasing the pH to 5. The observed behaviour resembles that of
9 humic and fulvic acids complexation with Ca^{2+} ions.¹⁴
10

11 *Synthesis of hydroxyapatite magnetic nanoparticles*

12 A modification of literature methods was used for the synthesis of hydroxyapatite nanoparticles, nAp.¹⁵
13 Briefly, a suspension of $\text{Ca}(\text{OH})_2$ (5 g in 40 ml H_2O) was stirred and heated to 80 °C. A phosphoric acid
14 solution (4.44 g in 60 ml of H_2O) was added drop-wise into the calcium hydroxide suspension over a period
15 of 2 h under constant heating and stirring, to obtain a suspension of nAp. The precipitate was separated from
16 the mother liquor by centrifugation, washed several times with deionized water and dried at 80 °C.
17

18 The previous process was adapted for the synthesis of Fe-containing hydroxyapatite nanoparticles, denoted
19 as Fe-nAp. A $\text{FeCl}_2 \cdot 4\text{H}_2\text{O}$ (1.27 g), $\text{FeCl}_3 \cdot 6\text{H}_2\text{O}$ (1.79 g) phosphoric acid (4.44 g in 60 ml of H_2O) solution
20 was added drop-wise into a $\text{Ca}(\text{OH})_2$ suspension (5 g in 40 ml H_2O) over a period of 2 h under constant
21 stirring and heating at 80 °C. The total amounts of iron to calcium ions were adjusted to obtain an analytical
22 molar ratio of Fe/Ca = 0.2. The reaction products were kept in suspension with constant stirring for 24 h at
23 room temperature. The precipitate was separated from the mother liquor either by centrifugation or by means
24 of a laboratory magnet bar of c.a. 2000 G, then washed several times with deionized water and dried at 80
25 °C.
26

27 For the synthesis of SBO-templated iron-containing hydroxyapatite nanoparticles, either 20, 200, or 1000
28 mg of SBO were dissolved in a $\text{Ca}(\text{OH})_2$ suspension (5 g in 40 ml H_2O) and the resulting suspension stirred
29 for 2 hours at 80 °C. A $\text{FeCl}_2 \cdot 4\text{H}_2\text{O}$ (1.27 g), $\text{FeCl}_3 \cdot 6\text{H}_2\text{O}$ (1.79 g) phosphoric acid (4.44 g in 60 ml of H_2O)
30 solution was then added drop-wise into the $\text{Ca}(\text{OH})_2$ – SBO suspension over a period of 2 h under constant
31 stirring and heating at 80 °C. The reaction mixture was kept in suspension with constant stirring for 24 h at
32 room temperature. The precipitate was separated from the mother liquor by centrifugation and by means of a
33 laboratory magnet bar, and then washed several times with deionized water until no SBO was observed in
34 the washing liquors by, both, UV-vis spectroscopy and total organic carbon assays. All the particles were
35 dried at 80°C. The particles were named 0.05SBO-Fe-nAp, 0.5SBO-Fe-nAp, and 2.5SBO-Fe-nAp, according
36 to the SBO/Ca w/w ratio used in the synthesis. When required, 2.5SBO-Fe-nAp powders were further
37 calcined at 600 °C for 3 hours. Calcined particles are therefore named 2.5SBO-Fe-nAp-cal.
38
39

40 *Particle characterization*

41 The crystalline phase content of samples was assessed by X-ray Diffraction (XRD) by using a PW3040/60
42 X'Pert PRO MPD X-ray diffractometer from PANalytical, in Bragg-Brentano geometry, equipped with the
43 high power ceramic tube PW3373/10 LFF source with Cu anode. The qualitative phase analysis was
44 performed with the EVA software package and compared to the ICDD- PDF-2- database. The effect of Fe
45
46
47
48
49
50

1
2
3 and SBO treatment on nAp crystallites domain size, D_v , were evaluated. A lower limit value of D_v was
4 calculated employing the Scherrer equation relating the size of sub-micrometre particles in a solid to the
5 broadening of diffraction pattern main peaks¹⁷ and considering $k = 0.9$ as the shape factor and $\lambda = 0.154056$
6 nm as the wave length of the X-rays for Cu $K\alpha_1$ radiation.
7
8

9 High resolution transmission electron microscopy (HRTEM) studies were carried out on a JEOL JEM
10 3010UHR (300 kV) TEM fitted with a single crystal LaB_6 filament. Samples were dry deposited on Cu
11 “holey” carbon grids (200 mesh).
12

13 The thermal behaviour of the powders was studied by thermal gravimetric analysis (TGA) using a Q600
14 TA Instruments. The program used a nitrogen environment and involved a one minute initial temperature of
15 50 °C, followed by a 20 °C /min ramp up to 800 °C and maintained at this temperature for 10 minutes. For
16 some samples, an oxygen environment was also used.
17
18

19 The functional groups present in the prepared nanoparticles were identified by their IR spectrum obtained
20 with a Bruker IFS28 spectrophotometer equipped with a Globar source and a DTGS detector working at 128
21 scans with 4 cm^{-1} resolution in the overall range 4000–400 cm^{-1} . Samples were prepared by pressing a
22 grounded mixture of 1% of the particles powder with 99% dry KBr at a load of 5 tons.
23
24

25 Nitrogen gas-volumetric adsorption experiments for specific surface area determinations (BET model)
26 were performed at 77 K by means of a ASAP2020 by Micromeritics model. Before each measurement,
27 samples were outgassed overnight at 80 °C at a residual pressure of about 10^{-2} mbar to guarantee a good
28 cleaning of the sample surface.
29
30

31 The X-ray photoelectron spectroscopy (XPS) spectra were obtained under UHV with a XR50 Specs
32 GmbH spectrometer using Mg $K(\alpha)$ as the excitation source and a PHOIBOS 100 half sphere electron energy
33 analyzer. A two-point calibration of the energy scale was performed using sputtered cleaned gold (Au 4f7/2,
34 binding energy (BE) 84.00 eV) and copper (Cu 2p3/2, BE: 932.67 eV) samples. Internal calibration to
35 correct for surface charging was performed with the C 1s peak at BE= 284.6 eV due to adventitious carbon.
36 High resolution XPS spectra were taken to get a better insight into the chemical environment of the different
37 atoms. A Shirley-type background from each spectrum was used to remove the effect of the extrinsic
38 structure loss and the spectrum resolved by Gaussian-Lorentzian fitting, keeping χ^2 values to their
39 minimum values.
40
41

42 The electrophoretic mobility was measured by Laser Doppler Velocimetry- Photon Correlation
43 Spectroscopy using a DELSA 440 spectrometer (Beckman Coulter Electronics, Hialeah, FL) equipped with a
44 5 mW HeNe laser (632.8 nm).
45
46

47 The magnetic characteristics of the particles was assessed using a Lakeshore 7403 vibrating sample
48 magnetometer. Magnetization of dried samples was performed at room temperature up to a maximum field
49 of 1.9T.
50
51

52 Metal determinations were performed with a Perkin Elmer Optima 7000 DV Model inductively coupled
53 plasma atomic emission spectrometer (ICP-AES). The instrument is equipped with a Echelle
54 monochromator, a cyclonic spray chamber, and a PTFE Mira Mist nebulizer. The instrumental conditions
55
56
57
58
59
60

were: plasma power 1.3 kW; sample aspiration rate 1.2 mL/min; argon cooling flow 1.5 L/min; argon sampling flow 0.6 L/min. The overall P:Ca:Fe ratio of the synthesized particles was also measured by ICP after acid digestion of the particles.

Metal adsorption experiments

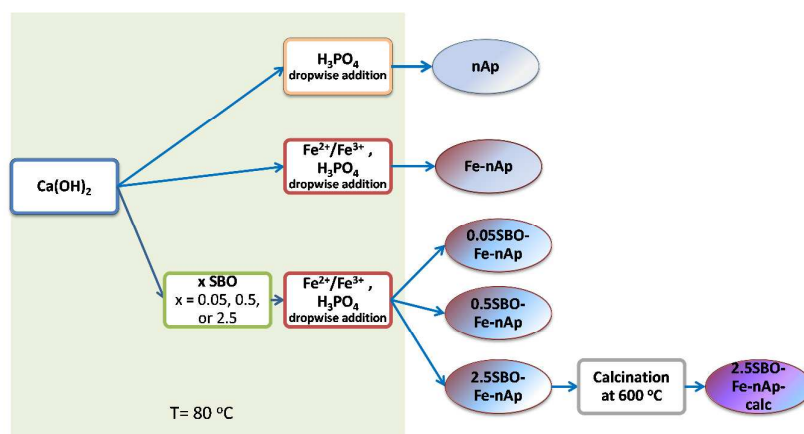
Adsorption studies were conducted in batch experiments. Variable ml-aliquots of a $\text{Cu}(\text{NO}_3)_2$ stock solution of 1000.0 mg L^{-1} were mixed with 5 ml of a 100 ppm solution of either nAp, Fe-nAp, 0.05SBO-Fe-nAp, 0.5SBO-Fe-nAp, 2.5SBO-Fe-nAp, or 2.5SBO-Fe-nAp-cal, and further diluted to a final volume of 25 mL with a solution of 4-(2-hydroxyethyl) piperazine-1-ethanesulfonic acid sodium salt (HEPES-Na) of pH 7 and 0.01 M ionic strength. The highest $[\text{Cu}^{2+}]$ used was limited by Cu^{2+} solubility.¹⁸

The suspensions were shaken at room temperature ($25 \pm 2^\circ\text{C}$) for several hours until equilibration was observed. Preliminary experiments showed that equilibration takes place already after one hour. The supernatant and solid residues were separated by centrifugation at 4,000 rpm for 10 min. The Cu concentration in the supernatant solutions was determined by ICP-AES. The amount of adsorbed Cu was calculated according to $x/m = v \times (C_o - C_e) / m$, where x/m (mg g^{-1}) is the weight in mg of Cu^{2+} ions adsorbed per g of particles, C_o and C_e (mg.L^{-1}) stand for the initial and equilibrium Cu^{2+} concentrations in solution, respectively, v (L) is the solution volume used in the experiment and m (g) is the mass of particles used. Data were expressed as the mean of three replicates.

Results and Discussion

A flow chart of the pathways followed for the synthesis of the different particles is described in Scheme 1.

Scheme 1: Flow chart of the synthesis pathways used for obtaining the different particles. “x” denotes the SBO/Ca w/w analytical ratio after mixing.



Particle characterization

The effect of SBO and Fe on the physical and chemical properties of nAp was studied and compared with untreated nAp. Figure 1 shows comparative HRTEM micrographs of the prepared powders. Due to

1
2
3 substantial agglomeration it is not possible to obtain a statistic analysis of the particles size. However, the
4 micrographs show cylindrical, 100 - 150 nm length, crystalline nAp particles, as indicated by the presence of
5 interference fringe patterns observable at high resolution. Fe-nAp particles show somewhat shorter (50 – 100
6 nm) acicular shapes of irregular contour. The latter observation is in line with the reported effect on the
7 morphology of rod-like nanometer size crystalline nAp which became elongated and the crystallinity slightly
8 lowered upon addition of Fe(III) ions,¹⁹ *vide infra*. Inhibition of hydroxyapatite *c*-axis and promotion of the
9 *a*-axis by added Fe(II) during a co-precipitation synthesis was also reported.²⁰

10
11
12
13
14 The use of 2.5 w(SBO)/w(Ca) as template in the synthesis of the particles leads to an even more
15 heterogeneous sample of irregular acicular particles. Calcination of 2.5SBO-Fe-nAp leads to an increased
16 size heterogeneity with a predominant population of enlarged particles. In all the micrographs relative to Fe-
17 containing samples, it is possible to observe the presence of globular lumps characterized by higher optical
18 density assignable to iron-containing domains of nanometric size (< 10 nm), as also reported for Fe-
19 containing particles obtained by similar synthetic procedures.^{16,17} The lumps are distributed quite
20 homogeneously in the materials, indicating that the synthesis in the presence of Fe²⁺/Fe³⁺ salts brought about
21 a good dispersion of iron-containing phases on Ap-based materials. This characteristic seems to be enhanced
22 in the SBO patterned particles.
23
24
25
26

27
28 The XRD diffractograms of nAp-based materials are shown in Figure 2. Hydroxyapatite XRD patterns are
29 observed in all the prepared powders with no significant shifting of peak positions, thus suggesting that Fe²⁺/
30 Fe³⁺ incorporation did not greatly modify the hydroxyapatite structure. A marked broadening increase of the
31 XRD peaks of Fe-nAp, and particularly of 2.5SBO-Fe-nAp and 2.5SBO-Fe-nAp-cal powders, strongly
32 indicates an important reduction in the crystalline structure of the particles. In addition, these samples exhibit
33 more intense diffraction peaks at $2\theta = 35.5$, as well as peaks of lower intensity at $2\theta = 30.2$ and 62.5 ,
34 characteristic of magnetite and maghemite structures (depicted in figure 2). Despite the presence of
35 magnetite and maghemite crystalline phases is being supported, they could not be unambiguously
36 differentiated, since their XRD diffraction spectrum mainly differ in the relative intensity of the peaks. In
37 fact, the obtained XRD data closely resembles those reported for Fe-containing hydroxyapatites from
38 different synthetic methods.^{15, 16, 21}
39
40
41
42
43
44

45 Figure 1: HRTEM micrographs. Circles show iron-containing domains.
46
47
48
49
50
51
52
53
54
55
56
57
58
59
60

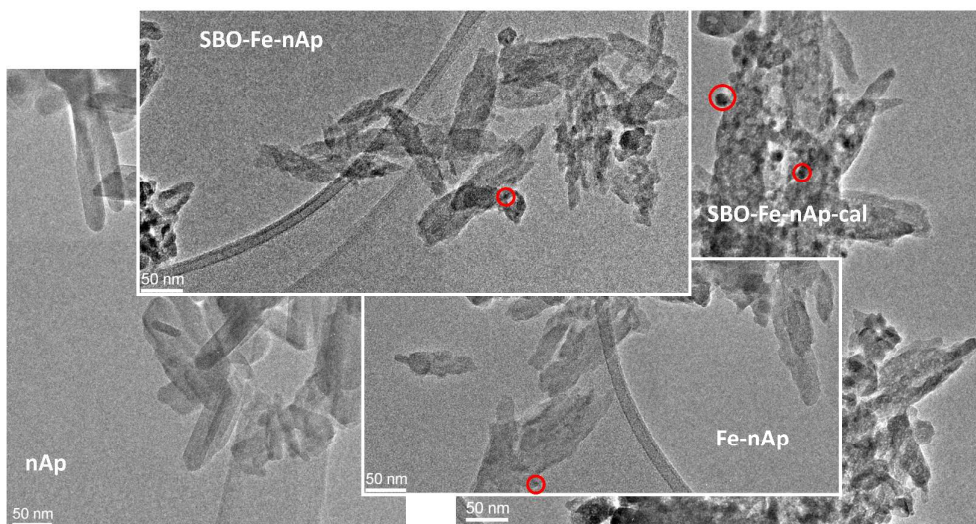
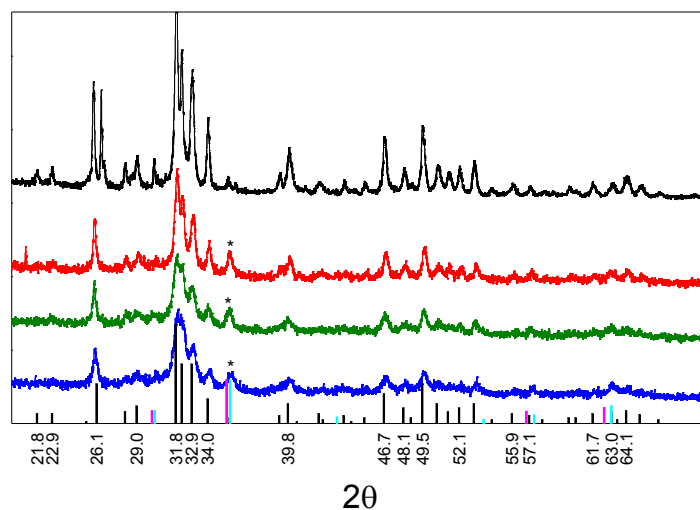


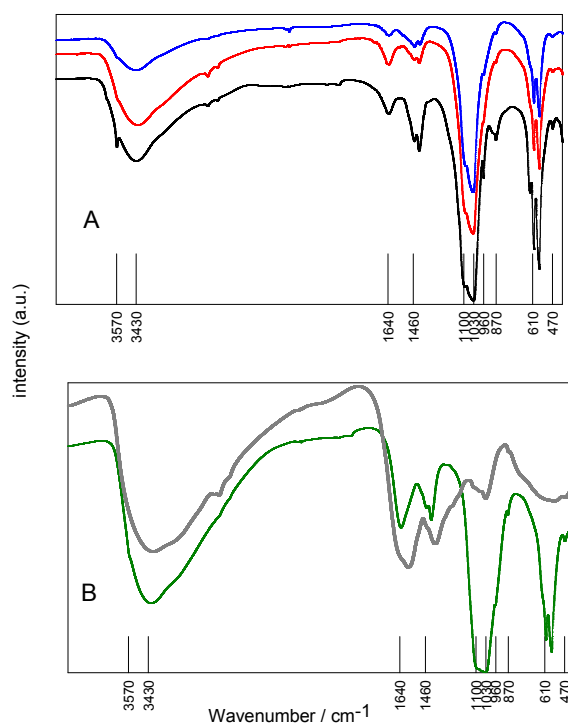
Figure 2: X-ray diffractograms of (from top to down) nAp, Fe-nAp, 2.5SBO-Fe-nAp, and 2.5SBO-Fe-nAp-cal. Bars stand for hydroxyapatite (black), maghemite (cyan), and magnetite (pink) principal reference patterns. Astericks indicate the $2\theta = 35.5$ diffraction peak.



The FTIR spectra of the particles are shown in Figure 3. nAp spectrum shows the fundamental vibration modes of PO_4 groups of the apatitic structure at about 470, 560, 610, 960 and $1030\text{--}1100\text{ cm}^{-1}$.²² Moreover, the band at 870 and 1460 cm^{-1} attributed to residual carbonate from the synthesis process are also observed. The broad bands in the regions 1640 and 3430 cm^{-1} correspond to $\delta\text{H-O-H}$ bands and νOH signals due to HOH bands of lattice and physisorbed water molecules. The IR spectrum of Fe-nAp shows mainly peaks attributed to nAp. The characteristic peaks due to iron oxides in the $600\text{--}400\text{ cm}^{-1}$ range²³ may be occluded by those of nAp due to the low amount of iron present in the samples. The 2.5SBO-Fe-nAp spectrum shown in Figure 3B evidences nAp signals overlapped to those of SBO (also shown in the figure). The intense

bands at 3430 and 1649 cm^{-1} indicates the presence of HO groups of phenols, alcohols and carboxyl groups, and of C=O bonds of carboxyl and carbonyl moieties, respectively. On the other hand, the FTIR absorption peaks of 2.5SBO-Fe-nAp-cal may be assigned mainly to those of nAp, thus indicating that 3 hours calcination at 600 $^{\circ}\text{C}$ of 2.5SBO-Fe-nAp powders is effective in eliminating SBO residues. nAp spectrum also shows the sharp hydroxyl bands at 632 and 3572 cm^{-1} , typical of nAp with a high degree of crystallinity. The absence of these peaks in the spectra of all the other particles suggests that the powders show poor crystallinity, in agreement with XRD data also supporting a decreased hydroxyapatite crystallinity upon Fe addition and use of SBO as organic template.

Figure 3: FTIR spectra (from down to top): (A) nAp, Fe-nAp, and 2.5SBO-Fe-nAp-cal. (B) SBO and 2.5SBO-Fe-nAp.



The TGA curves (see Figure 4) obtained in a N_2 environment in the temperature range from 80 to 800 $^{\circ}\text{C}$ for Ap-based materials yield information on the adsorbed substrates, as decomposition of the Ap structure is expected at temperatures over 900 $^{\circ}\text{C}$.²² The 5.9 % total mass loss of nAp is attributed to adsorbed water ($T \leq 100$ $^{\circ}\text{C}$), dehydration of hydroxides (380 -500 $^{\circ}\text{C}$), and elimination of surface carbonate-like groups (500 - 800 $^{\circ}\text{C}$), in good agreement with literature reports for nano-sized Ap powders.²² Fe-nAp shows an 8% total mass loss between 80 and 800 $^{\circ}\text{C}$ attributed to adsorbed water, dehydration of Fe hydroxides (380 -500 $^{\circ}\text{C}$), and elimination of surface carbonate-like groups. On the other hand, 2.5SBO-Fe-nAp powder shows a 14 %

total mass loss suggesting an important contribution of SBO pyrolysis (curve not shown), in agreement with the fact that only a 4 % weight loss is observed for the same particles calcined for three-hours at 600 °C. The latter observations are in agreement with the FTIR spectra indicating the presence of SBO in 2.5SBO-Fe-nAp, and a complete elimination of the organic template in the calcined powders. An estimation of the particles carbon content may be obtained from the mass loss in the temperature range from 200 to 380 °C observed in TGA curves performed in O₂ environment. Approximately 5% mass content due to SBO is estimated for 2.5SBO-Fe-nAp. TGA curves of 0.5SBO-Fe-nAp and 0.05SBO-Fe-nAp performed in the presence of O₂ agree, within the experimental error, with that of Fe-nAp, indicating that no significant amounts (< 1%) of organic matter is present in the materials.

Figure 4: TGA performed in a N₂ atmosphere, curves (A) nAp, (B) Fe-nAp, and (C) 2.5SBO-Fe-nAp-cal. TGA performed in an O₂ atmosphere, curves (D) 0.05SBO-Fe-nAp, (E) 0.5SBO-Fe-nAp, and (F) 2.5SBO-Fe-nAp. Corresponding derivative curves are shown in S1.

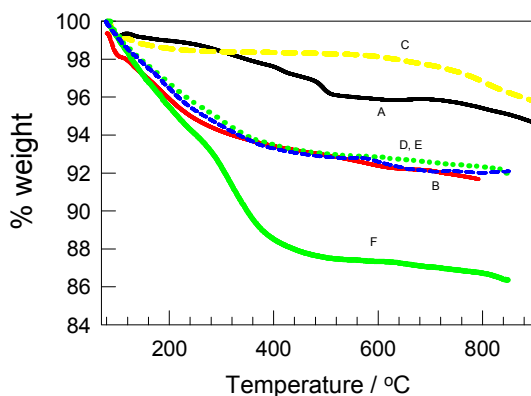


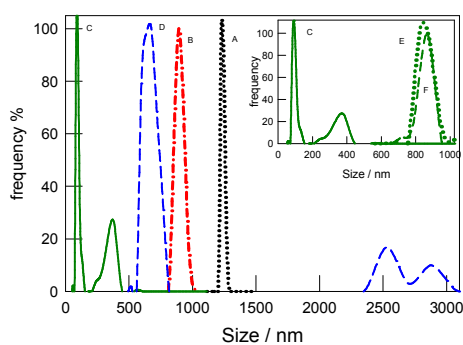
Table 1 depicts the specific surface area of the synthesized powders as determined by BET model and the relative crystallites domain size as estimated by Scherrer equation using the XRD data. Crystalline nAp shows the lowest surface area while almost a twofold increase is observed for Fe-nAp, and a further 15% increase is observed for 2.5SBO-Fe-nAp. Calcination of the latter reduces the surface area by 15%. The BET isotherms show hysteresis mainly at high P/P^0 values related to N₂ condensation inside inter-particle macropores of ca. 100 nm (see S2). Crystallite domain sizes decrease in the trend nAp < Fe-nAp < 2.5SBO-Fe-nAp while a further increase is observed for 2.5SBO-Fe-nAp-cal. All together, the results suggest a reduced crystallite domain size with increasing specific surface area and particle size diminution. The increase of specific surface area besides crystallinity diminution is also reported for nanoparticulated apatite.²⁴

Table 1: Specific surface area as obtained from BET isotherms, lower limit size as estimated by the Scherrer equation, surface stoichiometric ratio obtained by XPS analysis, % C from TGA experiments, electrophoretic mobility (μ) in the pH range from 6.5 to 7, bulk Ca and Fe percentages, and Fe to Ca molar ratio in the particle bulk.

Particle Type	Specific surface area /m ² g ⁻¹	crystallite domain size/nm	Surface composition	% w/w SBO	μ (mS/cm)	bulk		
						% Ca w/w	% Fe w/w	Fe/Ca
nAp	34	30–50	Ca ₁ P _{0.7} O _{3.1} Fe ₀	0	+0.95	38.4	< 0.02	0
Fe- nAp	64	20-40	Ca ₁ P _{0.9} O _{4.6} Fe _{0.14}	0	-1.8	28.4	7.8	0.2
0.05SBO-Fe-nAp	68	----	----	< 1	-1.5	31.2	7.4	0.17
0.5SBO-Fe-nAp	70	----	Ca ₁ P _{0.7} O _{3.7} Fe _{0.09}	< 1	-1.6	29.0	6.9	0.17
2.5SBO-Fe-nAp	71	10-30	Ca ₁ P _{0.75} O _{3.7} Fe _{0.09}	~5	-1.8	28.3	6.6	0.17
2.5SBO-Fe-nAp-cal	64	20-60	Ca ₁ P _{0.8} O _{3.3} Fe _{0.06}	0	-----	30.9	7.2	0.17

The average hydrodynamic particle size distribution determined by DLS measurements, shown in Figure 5, indicates that the particles hydrodynamic sizes are several fold-times higher than the sizes observed in TEM micrographs. Thus, important aggregation in aqueous solutions at pH 7 and 0.01 M ionic strength takes place. The amount of SBO used as template in the particles synthesis strongly influences aggregation, as smaller hydrodynamic sizes are observed for increasing SBO concentrations. Calcination of 2.5SBO-Fe-nAp particles increases the aggregates size, in line with the population of larger particles depicted in the corresponding HRTEM micrographs (*vide supra*). Aggregate sizes in the range of 100 nm are observed for 2.5SBO-Fe-nAp particles, and interparticle macroporosity of almost the same size is evidenced by N₂ gas-volumetric adsorption, thus indicating that macropores formed in the solid state do not have real significance in aqueous suspensions of the particles.

Figure 5: Hydrodynamic particle size distribution as obtained by DLS for nAp (A), Fe-nAp (B), 2.5SBO-Fe-nAp (C), 2.5SBO-Fe-NA-cal (D), 0.5SBO-Fe-nAp (*inset*, E), and 0.05SBO-Fe-nAp (*inset*, F).



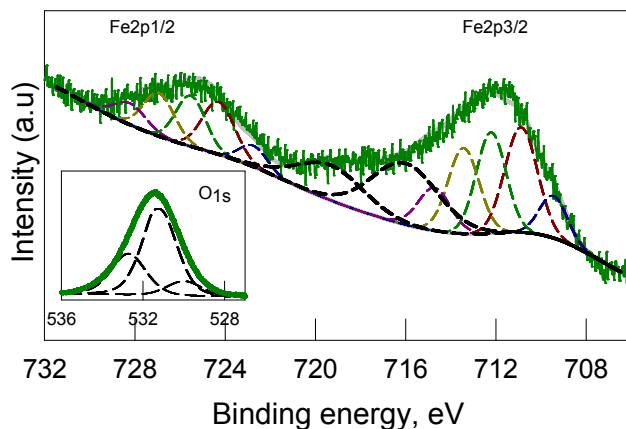
The electrophoretic mobility of the particles obtained in the pH range from 6.5 to 7 are depicted in Table 1. nAp and Fe-nAp values of +0.95 and -1.8 mS/cm, respectively, indicate that the incorporation of 20% Fe on the hydroxyapatite particles brings about an increased surface charge density and a predominance of negative surface charges. Moreover, SBO-patterned particles show electrophoretic mobilities similar to those observed for Fe-nAp. The contrast between the similar mobilities of these particles with their different

1
2
3 aggregates size strongly suggests an increased surface hydrophylicity in SBO-patterned particles due to the
4 presence of uncharged surface groups which strongly stabilize the aqueous suspensions of the particles.
5

6 The XPS survey spectra of the particles (see S4) depict the main lines for Ca, O, P, and Fe (except for
7 nAp). Beside these peaks, a C(1s) “adventitious carbon” peak was observed which was used for binding
8 energy correction due to charging effects by setting it to 284.6 eV. Carbonate-type carbon, incorporated
9 during synthesis, was also observed. All powders show the Ca2p_{1/2} (350.8eV) and Ca2p_{3/2} (347.4 eV)
10 lines, and the P2s line at 191 eV due to calcium phosphate in apatite (see S5). On the other hand, analysis of
11 Fe2p_{3/2} peaks is more controversial. The use of broad peak shapes has proved useful for the identification of
12 pure compounds but of lesser use for the identification of mixtures due to the spectral overlap of most Fe(III)
13 compounds which show similar binding energies but varying peak shapes and satellite intensities.²⁵ In fact,
14 such analysis leads to a peak at about 710.5 eV with a satellite displaced 4 eV and a second broad peak at
15 about 712.5 eV with no satellite contribution unless overlapped to the Fe2p_{1/2} portion of the spectrum.
16 These peaks did not match the reported data of neither pure Fe oxides²⁶ nor of phosphated iron.²⁷ Therefore,
17 Fe2p_{3/2} peaks for all the iron-containing samples herein synthesized were modelled using a combination of
18 ferrous and ferric multiplet patterns for the lower and higher energy portion of the spectrum, respectively,^{25,}
19 ²⁸ as shown in Figure 6 for Fe-nAp. Fe2p_{3/2} signal adjustment was performed assuming a Shirley type
20 baseline and using the lowest number of peaks allowed with about 1.7 eV FWHM, except for the peak
21 attributed to Fe II satellite which was left free. All samples show contributing peaks at 709.5, 710.9, 712.2,
22 713.4, 714.9 eV, and Fe²⁺ satellite peak shifted by 4.8- 5 eV, in line with the patterns reported for Fe(II)-PO₄
23 surface oxidized to Fe(III)-OH.²⁸ Moreover, no metallic component can be observed in the spectrum
24 indicating its absence in the surface layer. The observed satellite peak at c.a. 719 eV, may be assigned to the
25 contribution of iron oxides.^{26, 29} Observed Fe2p_{3/2} and Fe2p_{1/2} signals separations, ΔE (BE 2p_{3/2} –BE
26 2p_{1/2}), of about 13.0–13.3 eV are in agreement with reported data for Fe oxides and salts.²⁶ Therefore, the
27 XPS data points to a complex mixture of Fe²⁺ / Fe³⁺ phosphates and oxides on the particles surface.
28
29
30
31
32
33
34
35
36
37
38
39

40 Deconvolution of the O1s peak of n-Ap shows the main contribution of a band at 531.8 eV (96%) and a
41 minor contribution at 532.8 eV. According to literature reports, these peaks may be assigned to oxygen
42 atoms in phosphates and hydroxyls, and to adsorbed water, respectively, in agreement with reported data for
43 hydroxyapatite.²⁷ On the other hand, O1s peaks of Fe-containing particles are best modelled when the
44 contribution of a third peak at c.a. 530.1 eV characteristic of O atoms in iron oxide environments is
45 considered,²⁶ as depicted in Figure 6 *inset* and S5. Peak contributions of 22 % and 13% were observed for
46 Fe-nAp and 2.5SBO-Fe-nAp-cal, respectively, while contributions of c.a. 5% were observed for 0.5SBO-
47 Fe-nAp and 2.5SBO-Fe-nAp. The latter observations are in line with the larger peak area of Fe2p_{3/2}
48 multiplets of BE > 711 eV observed for Fe-nAp and 2.5SBO-Fe-nAp-cal, normally identified with Fe³⁺ ions.
49
50
51
52
53

54 Figure 6: XPS Fe2p_{3/2} and Fe2p_{1/2} signals (full line) for 2.5SBO-Fe-nAp and contributing peaks (dashed
55 lines). *Inset*: O1s signals (full line) and contributing species (dashed lines).
56
57
58
59
60



Considering the experimental sensitivity factors relative to the different elements, a surface Ca:P:O stoichiometric ratio was determined for each particle type as depicted in Table 1. The P/Ca ratio for nAp is somewhat higher than the expected theoretical $\text{Ca}(\text{PO}_4)_{0.6}\text{O}_{0.2}$ stoichiometric ratio but close to the values reported in the literature for several hydroxyapatite materials and attributed to the presence of surface acid phosphates.²⁹ On the other hand, the O/P ratio is, within the experimental error, in line with the expected value for hydroxyapatite. Fe-nAp shows higher P/Ca and O/Ca ratios than nAp. All together, the data seems to indicate that surface iron increases phosphate content due to the formation of Fe(II)-phosphates while surface Fe^{3+} seems to lead to the formation of iron oxides. In fact, Fe(III)-substituted hydroxyapatite nanoparticles were reported to show an increased surface hydrophilicity as a consequence of the formation of surface Fe-OH groups, though the number of original Ca(II) atoms was reduced.¹⁹

On the other hand, lower Fe/Ca surface ratios were observed when SBO was used as template in the particle synthesis. 0.5SBO-Fe-nAp and 2.5SBO-Fe-nAp show P/Ca ratios similar to those of nAp, though the respective O/Ca ratios are significantly higher, thus suggesting the presence of surface OH groups. Upon calcination, 2.5SBO-Fe-nAp show a decreased content in surface oxygen and iron.

Hysteretic M-H curves of Fe-nAp and 2.5SBO-Fe-nAp at 300K (see S3) exhibit a superparamagnetic behavior with zero coercivity and zero remanence on the magnetization curves. For both particles, the saturation magnetization was of 4 emu/g of particles, in line with reported values for Fe-nAp nanopowders.¹⁵ Considering a 7% w/w iron content in the particles (see Table 1), the saturation magnetization per gram of iron is 57 emu/g Fe, half the value expected for magnetite nanoparticles.³⁰ Therefore, formation of significant amounts of iron compounds not contributing to the overall paramagnetism is supported.

The described results clearly indicate that introduction of Fe^{3+} / Fe^{2+} ions and the use of SBO- Ca^{2+} complexes as templates during hydroxyapatite synthesis leads to a diminution in the apatite crystalline structure, a negatively charged surface, and an increased surface hydrophilicity. Formation of magnetite and/or maghemite is observed by XRD. However, iron oxides formation is not the only fate of iron. The loss of crystallinity of the apatite structure might be a consequence of Ca^{2+} exchange by Fe^{2+} / Fe^{3+} ions. In fact, XPS analysis clearly indicates the presence of surface Fe^{2+} phosphates salts and oxidized Fe^{3+} . Formation of

surface FeO and OH groups is suggested from the O2s peak analysis. A comparison between Fe:Ca contents in the particles volume and at the surface, see Table 1, indicates that Fe ions are preferentially incorporated in the particles core.

Metal adsorption capacity

Figure 7 shows the measured Cu^{2+} adsorption isotherms. The one-adsorption site Langmuir model, eq. (1), fits the isotherms of Cu^{2+} adsorption on nAp, Fe-nAp, 0.05SBO-Fe-nAp, and 0.5SBO-Fe-nAp with regression coefficients $r^2 > 0.95$. The obtained fitting parameters are depicted in Table 2. The affinity coefficient of Cu^{2+} adsorption, k_L , shows the trend $\text{nAp} \approx \text{Fe-nAp} > 0.05\text{SBO-Fe-nAp} \approx 0.5\text{SBO-Fe-nAp}$ while the maximum number of sites b increases in the order $\text{nAp} < \text{Fe-nAp} < 0.05\text{SBO-Fe-nAp} < 0.5\text{SBO-Fe-nAp}$. On the other hand, adsorption on 2.5SBO-Fe-nAp and 2.5SBO-Fe-nAp-cal particles were better fitted by the Freundlich model, eq. (2). This experimental isotherm has been interpreted to arise from an heterogeneous surface showing a distribution of different adsorption sites, where $1/n \leq 1$ is an experimentally determined exponent and k_F the Freundlich constant. However, within the experimental error, obtained values of n are close to 1, thus suggesting the applicability of the Langmuir isotherm under the condition $1 \gg k_L \times C_e$ and $k_F = k_L \times b$. In fact, the maximum Cu^{2+} absorption could not be reached for these particles due to the limited Cu^{2+} solubility.¹⁸ Taking $k_L \times b = 90 \text{ mg g}^{-1}$ for 2.5SBO-Fe-nAp and considering $k_L \approx 0.11$ for SBO-templated particles (*vide supra*), results $b \approx 850 \pm 400 \text{ mg g}^{-1}$.

$$x/m = \frac{k_L \times b \times C_e}{1 + k_L \times C_e} \quad \text{eq.(1)}$$

$$x/m = k_F \times C_e^{1/n} \quad \text{eq.(2)}$$

Figure 7: Cu^{2+} adsorption isotherms at 25 °C. Main figure: Fe-nAp (●), 0.05SBO-Fe-nAp (∇), and 0.5SBO-Fe-nAp (■). *Inset left*: 2.5SBO-Fe-nAp (Δ), and 2.5SBO-Fe-nAp-cal (●). *Inset right*: nAp (○). The solid lines and dashed lines stand to the fitting of the data to eq.(1) and (2), respectively.

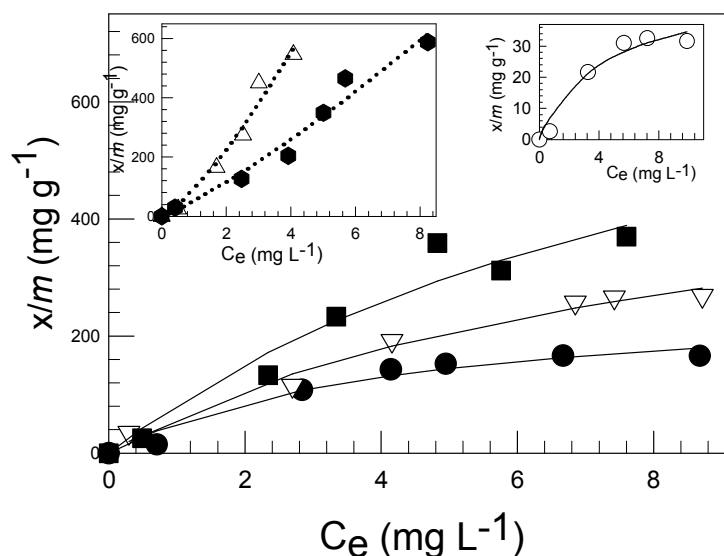


Table 2: Fitting parameter values of the Langmuir and Freundlich models. Error bars are denoted in parentheses.

Particle	eq.	$b / \text{mg g}^{-1}$	k_L	$1/n$	$k_F / \text{mg g}^{-1}$	r
nAp	1	50(25)	0.22(0.1)			0.967
Fe-nAp	1	265(60)	0.24(0.02)			0.969
0.05SBO-Fe-npA	1	550(200)	0.12(0.04)			0.978
0.5SBO-Fe-nAp	1	850(400)	0.10(0.07)			0.953
2.5SBO-Fe-nAp	2			1.3(0.2)	90(22)	0.974
2.5SBO-Fe-nAp-cal	2			1.2(0.2)	50(15)	0.970

Isolation of the Cu^{2+} -adsorbed nAp, Fe-nAp, and 0.5SBO-Fe-nAp and further resuspension in an aqueous solution of pH 7, show 0.2, 0.1, and 0.02 % Cu^{2+} leaching after two hours, respectively. Thus indicating that Cu^{2+} is strongly chemisorbed at pH 7.

The obtained value of b for nAp is in line with that reported for Cu^{2+} adsorption on commercial nanohydroxyapatite at pH 7.2 (64.8 mg g^{-1}), though the reported² $k_L = 0.80$ is almost 4 times higher than that found here. An even number of regularly spaced, positively charged, calcium ions and negatively charged oxygen groups on the surface of crystalline Ap support metal cation retention due to ion exchange and/or coordination with P-sites and surface HO. Moreover, Cu^{2+} precipitation with free PO_4^{3-} ions as a consequence of the high Ap solubility at pH 5 is also reported.³¹ In our experiments, the amounts of calcium and iron ion concentrations measured in solution during the Cu^{2+} adsorption experiments are *c.a.* 17 and 0.5

1
2
3 $\mu\text{g/g}$ NP, respectively, for all the particles, independently of the adsorbed amount of Cu^{2+} ions. Therefore,
4 Cu^{2+} exchange for Ca^{2+} and Fe^{2+} in the hydroxyapatite structure seems not to significantly contribute to Cu^{2+}
5 adsorption under our experimental conditions.
6

7
8 Moreover, the observed increase in the specific surface area of Fe-nAp and SBO-Fe-nAp containing
9 particles seems not to be the cause of the increased Cu^{2+} adsorption of these materials (*vide infra*), as
10 normalization of the adsorption isotherms by the specific surface area of the materials does not modify the
11 observed trend.
12

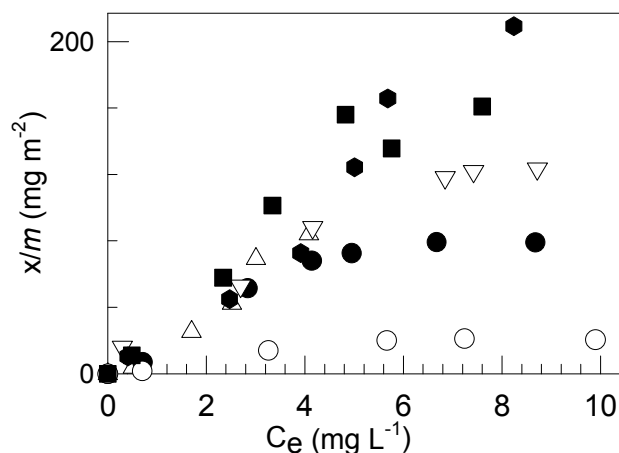
13
14 Reported Cu^{2+} maximum adsorption capacities for different magnetite composites are of the order of 1.9
15 for aqueous suspensions of pH 5.5,³² 56.71 for magnetite-immobilized chitin,³³ and 140-150 mg/g for
16 magnetite-immobilized *pseudomonas putida* 5X cells at pH 7.³² These values are below those observed for
17 the materials herein synthesized. On the other hand, Cu^{2+} ions have been reported to readily form non-labile
18 complexes with fulvic acids and dissolved natural organic matter, DOM,³⁴ as amino groups, phenolic
19 hydroxyls and adjacent aromatic carboxylates provide lone pairs of electrons for chelating Cu^{2+} ions. The
20 reported total number of binding sites range from 1 to 100 $\mu\text{M mgC}^{-1}$ depending on pH, ionic strength, and
21 the DOM origin and concentration. A rough estimation of the adsorption sites provided by SBO may be
22 obtained if it is considered that 5% mass of 2.5SBO-Fe-nAp is due to SBO organic residues, from which
23 38.5 % in weight is due to C atoms. Therefore, taking the maximum amount of 100 μM sites mgC^{-1} , ~122 mg
24 g^{-1} Cu^{2+} ions would be adsorbed by the organic matter, well below the obtained values (see Table 2).
25 Consequently, the increased Cu^{2+} adsorption capacity observed for SBO-patterned particles cannot be
26 assigned solely to surface-trapped SBO, neither to the small magnetite domains observed on the particles
27 surface. These observations are further supported by the significant Cu^{2+} adsorption capacity still observed
28 for 2.5SBO-Fe-nAp-cal despite the elimination of all C-containing residues due to calcination.
29
30
31
32
33
34
35
36

37
38 As discussed above, the main differences observed between nAp and Fe-containing apatites involve a
39 reduction in the crystallinity of hydroxyapatite domains, a reduced Ca^{2+} content, and the formation of surface
40 phosphated iron and magnetite/maghemite phases. An increased O-content is also observed at the surface of
41 all SBO-Fe-nAp materials. Such surface and structural modifications might support an increased adsorption
42 efficiency of the iron-containing hydroxyapatite materials due to Cu^{2+} complexation with surface PO_4 and OH
43 groups. It results striking though, that despite both 0.5SBO-Fe-nAp and 2.5SBO-Fe-nAp showing similar
44 surface composition, except for the small C content of the latter, Cu^{2+} adsorption ability of 2.5SBO-Fe-nAp
45 is significantly higher. We suggest therefore, that the smaller aggregates formed by 2.5SBO-Fe-nAp in
46 aqueous suspensions makes the particles surface more available for Cu^{2+} adsorption. In fact, strong
47 electrostatic interactions might prevent Cu^{2+} ions to approach the binding sites of the particles surface within
48 the aggregates. Surface area measurements of dry materials do not necessarily represent the effective surface
49 area of suspended particles in aqueous solution because of the particles agglomeration in suspension.^{35, 36}
50
51
52
53
54

55
56 A rough estimation of the effective surface area may be obtained if it is assumed that Cu^{2+} is mainly
57 adsorbed at the agglomerates surface, and taking the agglomerates hydrodynamic radius distribution
58
59
60

measured by DLS and the density value of hydroxyapatite (3.156 g/cm^3)³⁷ for all the particles. Normalization of the isotherms shown in Figure 6 by the estimated effective agglomerate area (1.55, 2.1, 2.2, 2.3, 6.5, and $2.8 \text{ m}^2\text{g}^{-1}$ for nAp, Fe-nAp, 0.05SBO-Fe-nAp, 0.5SBO-Fe-nAp, 2.5SBO-Fe-nAp, and 2.5SBO-Fe-nAp-cal, respectively) yields adsorption isotherms (see Figure 8) which may be classified in two main groups: nAp and Fe-containing apatites. Iron-containing particles, all depicting similar k_L values, show improved adsorption capacity with respect to pure nAp, in line with their described surface characteristics, *vide supra*. Differences among the adsorption isotherms of the iron-containing particles are mainly observed at high Cu^{2+} loadings, probably due to Cu^{2+} adsorption on the particles surface facing the interior of the agglomerates at higher concentrations, a situation not considered in the simplified estimation of the effective surface area.

Figure 8: Cu^{2+} adsorption isotherms at $25 \text{ }^\circ\text{C}$ normalized by the effective area (see text). nAp (\circ), Fe-nAp (\bullet), 0.05SBO-Fe-nAp (∇), 0.5SBO-Fe-nAp (\blacksquare), 2.5SBO-Fe-nAp (\triangle), and 2.5SBO-Fe-nAp-cal (\blacklozenge).



Conclusions

The present results strongly indicate that hydroxyapatite nanoparticles doped with iron and synthesized using SBO as template, show significant changes in the particles morphology and surface chemistry. Among the observed effects are: a reduction in the crystallinity of hydroxyapatite domains, elongated and smaller particles with higher specific surface area, reduced Ca^{2+} content, formation of surface phosphated iron and iron oxides, increased oxygen content at the surface, and an overall negative surface charge at pH 7.0. Moreover, formation of magnetite oxide seems responsible for the particle paramagnetism. Such surface and structural modifications support the formation of stable homogeneous aqueous suspensions of the particles,

1
2
3 which show a reduction in the size of the agglomerates when increasing the SBO content in the synthesis
4 procedure.
5

6 A significant improvement in the Cu^{2+} adsorption capacity was observed upon iron-doping of the
7 hydroxyapatite particles and, particularly, for the SBO-templated particles. Such improvement is correlated
8 with a negatively-charged surface and the presence of phosphate and Fe-OH surface groups. However, a
9 second important effect appears to be the agglomerates size, as agglomeration seems to severely reduce the
10 effective surface available for adsorption in aqueous suspensions.
11

12 The materials herein synthesized are a potential, self-sustaining, environmentally friendly, and efficient
13 material for Cu^{2+} remediation in aqueous effluents. Future work involves metal sorption selectivity studies
14 and metal desorption conditions for particle reuse.
15
16
17

18 **Aknowledgement**

19 D.F.M. thanks Consejo Nacional de Investigaciones Científicas y Técnicas (CONICET, Argentina) for a
20 graduate studentship. M.C.G. is a research member of CONICET. The work was performed partly with
21 funds of the Ministero Italiano delle Politiche Agricole within the Agrienergia project and by the grant PIP
22 112-200801-00356 from CONICET, Argentina. Financial support for academic interchange by the European
23 Union (IRSES-GA-2010-269128, EnvironBOS) is acknowledged. The authors are grateful to the following
24 private and/or public Italian institutions: (a) AceaPinerolese Spa in Pinerolo (TO) for supplying the SBO
25 sourcing biowastes; (b) Studio Chiono and Associati in Rivarolo Canavese (TO) for making available pilot
26 equipment and services for the production of SBO. Beatriz Soria and Simona Sapino are acknowledged for
27 the TGA in presence of molecular oxygen and DLS measurements, respectively.
28
29
30
31
32
33
34
35

36 **Supporting Information Available:** TGA derivatives, N_2 adsorption isotherms and BJH mesoporosity
37 analyses, magnetization curves, XPS survey spectra and elements high resolution peaks. This material is
38 available free of charge via the Internet at <http://pubs.acs.org>.
39
40
41

42 **References**

- 43 (1) Moreno, J. C.; Gómez, R.; Giraldo, L. Removal of Mn, Fe, Ni and Cu Ions from Wastewater Using Cow
44 Bone Charcoal. *Materials* **2010**, *3*, 452-466.
45
46
47
48 (2) Wang, Y.; Zhou, D.; Cui Y.; Wang, S.; Chen, Y. Adsorption and Desorption of Cu(II), Zn(II), Pb(II), and
49 Cd(II) on the Soils Amended with Nanoscale Hydroxyapatite. *Environ. Prog. & Sustainable Energy* **2010**,
50 *29*, 233- 241.
51
52
53
54 (3) Lee, Y.; Elzinga, E. J.; Reeder, R. Sorption Mechanisms of Zinc on Hydroxyapatite: Systematic Uptake
55 Studies and EXAFS Spectroscopy Analysis. *J. Environ. Sci. Technol.* **2005**, *39*, 4042-4048.
56
57
58
59
60

- 1
2
3 (4) Handley-Sidhu, S.; Renshaw, J. C.; Moriyama, S.; Stolpe, B.; Mennan, C.; Bagherias, S.; Yong, P.;
4 Stamboulis, A.; Paterson-Beedle, M.; Sasaki, K.; Pattrick, R. A.; Lead D. J. R.; Macaskie, L. E. Uptake of
5 Sr^{2+} and Co^{2+} into Biogenic Hydroxyapatite: Implications for Biomineral Ion Exchange Synthesis. *Environ.*
6 *Sci. Technol.* **2011**, *45*, 6985–6990.
7
8
9
10 (5) Shekhar, N.; Krishanu, B.; Bikramjit, B. Phase Stability and Microstructure Development in
11 Hydroxyapatite–Mullite System. *Scripta Mater.* **2008**, *58*, 1054–1057.
12
13
14 (6) Wang, D.; Paradelo, M.; Bradford, S. A.; Peijnenburg, W. J. G. M.; Chu, L.; Zhou, D. Facilitated
15 Transport of Cu with Hydroxyapatite Nanoparticles in Saturated Sand: Effects of Solution Ionic Strength and
16 Composition. *Water Res.* **2011**, *45*, 5905–5915.
17
18
19
20 (7) Pagenkopf, G.; Whitworth, C. Precipitation of Metal-Humate Complexes. *J Inorg. Nucl. Chem.* **1981**, *43*,
21 1219–1222.
22
23
24
25 (8) Baigorri, R.; Urrutia, O.; Erro, J.; Mandado, M.; Perez-Juste, I.; Garcia-Mina, J. M. Structural
26 Characterization of Anion-Calcium-Humate Complexes in Phosphate-Based Fertilizers. *ChemSusChem*
27 **2013**, *6*, 1245 – 1251.
28
29
30
31 (9) Boffa, V.; Perrone, D. G.; Montoneri, E.; Magnacca, G.; Bertinetti, L.; Garlasco, L.; Mendichi, R. A
32 Waste Derived Biosurfactant for the Preparation of Templated Silica Powders. *ChemSusChem* **2010**, *3*, 445 –
33 452.
34
35
36
37 (10) Kithva, P. H.; Grøndahl, L.; Kumar, R.; Martin, D.; Trau, M. An Organic Matrix-Mediated Processing
38 Methodology to Fabricate Hydroxyapatite Based Nanostructured Biocomposites. *Nanoscale* **2009**, *1*, 229–
39 232.
40
41
42
43 (11) Qu, X., Alvarez, P. J. J.; Li, Q. Applications of Nanotechnology in Water and Wastewater Treatment.
44 *Water Res.* **2013**, *47*, 3931–3946.
45
46
47
48 (12) Iwasaki, T.; Nakatsuka, R.; Murase, K.; Takata, H.; Nakamura, H.; Watano, S. Simple and Rapid
49 Synthesis of Magnetite/Hydroxyapatite Composites for Hyperthermia Treatments Via a Mechanochemical
50 Route. *Int. J. Mol. Sci.* **2013**, *14*, 9365–9378.
51
52
53
54 (13) Montoneri, E; Boffa, V; Savarino, P; Perrone, D; Ghezzi, M; Montoneri, C; Mendichi, R. Acid Soluble
55 Bio-Organic Substances Isolated from Urban Bio-Waste. Chemical Composition and Properties of Products.
56 *Waste Manage.* **2011**, *31*, 10–7.
57
58
59
60

1
2
3
4 (14) Christl, I. Ionic Strength- and pH-Dependence of Calcium Binding by Terrestrial Humic Acids.
5 *Environ. Chem.* **2012**, *9*, 89–96.
6
7

8
9 (15) Tampieri, A.; D' Alessandro, T.; Sandri, M.; Sprio, S.; Bertinetti, L.; Panseri, S.; Pepponi, G.;
10 Goettlicher, J.; Bañobre-López, M.; Rivas, J. Intrinsic Magnetism and Hyperthermia in Bioactive Fe-Doped
11 Hydroxyapatite. *Acta Biomater.* **2012**, *8*, 843-851.
12
13

14
15 (16) Panseri, S.; Cunha, C.; D'Alessandro, T.; Sandri, M.; Giavaresi, G.; Marcacci, M.; Hung, C.; Tampieri,
16 A. Intrinsically Superparamagnetic Fe-Hydroxyapatite Nanoparticles Positively Influence Osteoblast-like
17 Cell Behaviour. *J. Nanobiotechnol.* **2012**, *10*:32.
18
19

20
21 (17) Patterson, A. The Scherrer Formula for X-Ray Particle Size Determination. *Phys. Rev.* **1939**, *56*, 978–
22 982.
23
24

25
26 (18) Hidmi, L.; Edwards, M. Role of Temperature and pH in Cu(OH)₂ Solubility. *Environ. Sci. Technol.*
27 **1999**, *33*, 2607 – 2610.
28
29

30
31 (19) Kandori, K.; Toshima, S.; Wakamura, M.; Fukusumi, M.; Morisada, Y. Effects of Modification of
32 Calcium Hydroxyapatites by Trivalent Metal Ions on the Protein Adsorption Behavior. *J. Phys. Chem. B*
33 **2010**, *114*, 2399–2404.
34
35

36
37 (20) Morrissey, R.; Rodríguez-Lorenzo, L. M.; Gross K. A. Influence of Ferrous Iron Incorporation on the
38 Structure of Hydroxyapatite. *J. Mater. Sci.: Mat. Med.* **2005**, *16*, 387-392.
39
40

41 (21) Li, Y.; Nam, C. T.; Ooi, C. P. Iron(III) and Manganese(II) Substituted Hydroxyapatite Nanoparticles:
42 Characterization and Cytotoxicity Analysis. *J. Phys.: Conf. Series* **2009**, *187*, 012024.
43
44

45
46 (22) Cotescu, A.; Pasuk, I.; Ungureanu, F.; Dinischiotu, A.; Costache, M.; Huneau, F.; Galaup, S.; Le
47 Coustumer, P.; Predoi, D. Physico-Chemical Properties of Nano-sized Hexagonal Hydroxyapatite Powder
48 Synthesized by Sol-Gel. *Dig. J. Nanomater. Bios.* **2010**, *5*, 989 – 1000.
49
50

51
52 (23) Sing Li, Y.; Church, J. S.; Woodhead, A.L. Infrared and Raman Spectroscopic Studies on Iron Oxide
53 Magnetic Nanoparticles and their Surface Modifications. *J. Magn. Magn. Mater.* **2012**, *324*, 1543–1550.
54
55

- 1
2
3 (24) Lee, W.-H.; Loo, C.-Yee; Van, K. L.; Zavgorodniy, A. V.; Rohanizadeh, R. Modulating Protein
4 Adsorption onto Hydroxyapatite Particles Using Different Amino Acid Treatments. *J. R. Soc. Interf.* **2012**, *9*,
5 918-927.
6
7
8
9 (25) Biesinger, M. C.; Payne, B. P.; Grosvenor, A. P.; Laua, L. W. M.; Gerson, A. R.; Smart, R. St. C.
10 Resolving Surface Chemical States in XPS Analysis of First Row Transition Metals, Oxides and Hydroxides:
11 Cr, Mn, Fe, Co and Ni. *Appl. Surf. Sci.* **2011**, *257*, 2717–2730.
12
13
14 (26) Yamashita, T.; Hayes, P. Analysis of XPS Spectra of Fe²⁺ and Fe³⁺ Ions in Oxide Materials. *Appl. Surf.*
15 *Sci.* **2008**, *254*, 2441–2449.
16
17
18
19 (27) Grosseau-Poussard, J. L.; Panicaud, B.; Pedraza, F.; Renault, P. O.; Silvain, J. F. Iron Oxidation Under
20 the Influence of Phosphate Thin Films. *J. Appl. Phys.* **2003**, *94*, 784.
21
22
23
24 (28) Pratt, A. R. Vivianite Auto-Oxidation. *Phys Chem Miner.* **1997**, *25*, 24–27.
25
26
27 (29) Khachani, M.; Kacimi, M.; Ensuque, A.; Piquemal, J-Y; Connan, C.; Bozon-Verduraz, F., Ziyad M.
28 Iron–Calcium–Hydroxyapatite Catalysts: Iron Speciation and Comparative Performances in Butan-2-ol
29 Conversion and Propane Oxidative Dehydrogenation. *Appl. Catal. A- Gen.* **2010**, *388*, 113–123.
30
31
32
33 (30) Sun, S.; Zeng H. Size-Controlled Synthesis of Magnetite Nanoparticles. *J. Am. Chem. Soc.* **2002**, *124*,
34 8204-8205.
35
36
37 (31) Fernane, F.; Mecherri, M. O.; Sharrock, P.; Hadioui, M.; Lounici, H.; Fedoroff M. Sorption of
38 Cadmium and Copper Ions on Natural and Synthetic Hydroxylapatite Particles. *Mat. Charact.* **2008**, *59*, 554
39 – 559.
40
41
42
43 (32) Sze, K. F., Lu, Y. J.; Wong, P. K. Removal and Recovery of Copper Ion (Cu²⁺) from Electroplating
44 Effluent by a Bioreactor Containing Magnetite-Immobilized Cells of *Pseudomonas putida* 5X. *Resour.*
45 *Conserv. Recy.* **1996**, *18*, 175-193.
46
47
48
49 (33) Wong, K. S.; Wong, K. H.; Chung, W. K.; Wong, P. K. Adsorption of Copper Ion on Magnetite-
50 Immobilised Chitin. *Water Sci Technol.* **2007**, *56*, 135-143.
51
52
53
54 (34) Yamashita, Y.; Jaffe, R. Characterizing the Interactions Between Trace Metal and Dissolved Organic
55 Matter Using Excitation-Emission Matrix and Parallel Factor Analysis. *Environ. Sci. Technol.* **2008**, *42*,
56 7374–7379.
57
58
59
60

1
2
3
4 (35) Senna, M. Determination of Effective Surface Area for the Chemical Reaction of Fine Particulate
5 Materials. *Part. Part. Syst. Char.* **1989**, *6*, 163–167.
6
7

8
9 (36) Murray, A. R; Kisin, E. R; Tkach, A.V; Yanamala, N.; Mercer, R.; Young, S.H.; Fadeel, B.; Kagan, V.
10 E; Shvedov, A. A. Factoring-in Agglomeration of Carbon Nanotubes and Nanofibers for Better Prediction of
11 their Toxicity versus Asbestos. *Part. Fibre Toxicol.* **2012**, *9*, 10.
12
13

14
15 (37) De With, G.; Van Dijk, H. J. A.; Hattu, N.; Prijs, K. Preparation, Microstructure and Mechanical
16 Properties of Dense Polycrystalline Hydroxyapatite. *J. Mater. Sci.* **1981**, *16*, 1592.
17
18
19
20
21
22
23
24
25
26
27
28
29
30
31
32
33
34
35
36
37
38
39
40
41
42
43
44
45
46
47
48
49
50
51
52
53
54
55
56
57
58
59
60

1
2
3 *Contents Graphic*
4
5
6
7
8
9
10
11
12
13
14
15
16
17
18
19
20
21
22
23
24
25
26
27
28
29
30
31
32
33
34
35
36
37
38
39
40
41
42
43
44
45
46
47
48
49
50
51
52
53
54
55
56
57
58
59
60

